Journal of Alloys and Compounds 855 (2021) 157103

Contents lists available at ScienceDirect

Journal of Alloys and Compounds

journal homepage: http://www.elsevier.com/locate/jalcom

Hierarchical MnS@MoS_2 architectures on tea bag filter paper for flexible, sensitive, and selective non-enzymatic hydrogen peroxide sensors

N. Priyanga [a, b], A. Sahaya Raja [a, **], Mehboobali Pannipara [c], Abdullah G. Al-Sehemi [c], Siew-Moi Phang [d], Yang Xia [e], Shu-Yi Tsai [f], J. Annaraj [g], S. Sambathkumar [h], G. Gnana kumar [b, *]

[a] PG and Research Department of Chemistry, G.T.N Arts College-Autonomous, Dindigul, 624005, India
[b] Department of Physical Chemistry, School of Chemistry, Madurai Kamaraj University, Madurai, 625021, India
[c] Department of Chemistry, King Khalid University, Abha, 61413, Saudi Arabia
[d] Faculty of Applied Sciences, UCSI University, Cheras, 56000, Kuala Lumpur, Malaysia
[e] College of Materials Science and Engineering, Zhejiang University of Technology, Hangzhou, 310014, China
[f] Department of Materials Science and Engineering, Hierarchical Green-Energy Materials Research Center, National Cheng Kung University, Tainan, Taiwan
[g] Department of Materials Science, Madurai Kamaraj University, Madurai, 625021, India
[h] Department of Chemistry, Vivekanandha College of Arts and Sciences for Women, Elayampalayam, 637 205, Tamil Nadu, India

ARTICLE INFO

Article history:
Received 14 July 2020
Received in revised form
28 August 2020
Accepted 7 September 2020
Available online 15 September 2020

Keywords:
Analyte utilization rate
Core@shell architecture
Flexibility
Microcubes
Nanosheets

ABSTRACT

We report here the rational development of MnO_2 nanorods coated tea bag filter paper (TBFP) as a self-standing, bendable, and disposable electrochemical probe for the sensitive and selective H_2O_2 detection and addresses their challenges in H_2O_2 sensing *via* the replacement of 'O' with 'S' in the form of MnS microcubes and its core@shell architecture with MoS_2. The as-configured MnS@MoS_2/TBFP overwhelms the constrains of conventional electrochemical probes including time and cost consumed electrode surface renewability and catalyst loading progression, and the practice of an insulating binder. The hierarchical open porous architectures of MoS_2-shell favour the diffusion of H_2O_2 into the core-MnS microcubes, facilitating an analyte utilization efficacy at both the core and shell architectures. The impacts of core@shell morphological features, replacement of 'O' with 'S', surface defects, and lattice distribution of MnS@MoS_2 toward non-enzymatic H_2O_2 sensing performances are elucidated using variant electrochemical techniques. With the synergism of uniformly implanted and exposed metallic active sites, efficient electron transfer rate, and high analyte utilization efficiency, MnS@MoS_2/TBFP exposes the low detection limit (120 nM), excellent sensitivity (650 μA mM^{-1} cm^{-2}), and wide linear range (500 nM-5 mM) on H_2O_2 detection. Furthermore, the scrutinized non-enzymatic H_2O_2 detection concerts of MnS/MoS_2/TBFP are selective, decisive, repeatable, and stable, constructing the excellent recovery rates in human urine sample analyses. Thus, the collective benefits of free-standing, flexible, binder-less, re-functional, and cost-efficient MnS@MoS_2/TBFP probe actualize the evolution of affordable and high performance H_2O_2 sensors.

1. Introduction

The effectual oxidizing and reducing characteristics of hydrogen peroxide (H_2O_2) construct its prospective applications in a number of chemical, food, pharmaceutical, clinical, and textile industries [1–3]. However, the inevitable disclosure of H_2O_2 renders pathological disorders in humans including malfunction of deoxyribonucleic acid (DNA), cardiovascular, diabetics, carcinogenesis, renal diseases, ageing etc., driving the development of accurate, simple, durable, sensitive, cost effective, and selective H_2O_2 diagnosis devices [4,5]. Compared to the prevailing H_2O_2 detection methods, non-enzymatic electrochemical technique has elucidated

* Corresponding author.
** Corresponding author.
E-mail addresses: spsahayamdgl@gmail.com (A.S. Raja), kumarg2006@gmail.com (G.G. kumar).

https://doi.org/10.1016/j.jallcom.2020.157103
0925-8388/

massive inquisitiveness, owing to its good selectivity, high sensitivity, anti-interference ability, lower detection limit, and possibility for miniaturization [6,7].

However, the catalytic reduction of H_2O_2 at conventional bare electrodes require large over potential and demonstrate sluggish electrokinetics, owing to their limited electrical conductivity and surface area [8,9]. It obviates the modification of conventional electrodes with catalytic structures to curtail the over potential. Although precious metal nanocatalysts (Au [10], Pt [11], Pd [12], and Ag [13]) were exploited for H_2O_2 detection, their constraints including scarcity, surface poisoning, and fouling incarcerated their scale-up processes [10–13]. Hence, several research accomplishments have been consummated on non-precious metal nanostructures including CuO [14], SnO_2 [15], Fe_2O_3 [16], CdO [17], Co_3O_4 [18], NiO [19], MnO_2 [20], and ZnO [21] for effectual H_2O_2 sensing. Amid the above, MnO_2 has drawn momentous consideration in H_2O_2 detection because of its constructive features of earth-abundant, cost-efficient, non-hazardous, low band gap energy (1.0–1.3 eV), rational electrical conductivity, small radial diameter, and elevated tunnel size (4.6 - 7.0 Å) [22–24]. In this line, MnO_2 nanorods on glassy carbon electrode (GCE) manifested the moderate sensitivity of 2.74 μA mM^{-1} toward non-enzymatic H_2O_2 sensing [25]. Babu et al., explored the morphological influences of MnO_2 nanostructures including nanorods, nanobelts, and nanoflowers on H_2O_2 detection [26]. Although MnO_2 nanorods demonstrated better H_2O_2 sensing performance compared to those of nanobelts and nanoflowers due to the maximum adsorption of H_2O_2 in the large tunnel size of nanorods, the acquired sensing performance was not adequate enough for practical applications, owing to the limited electrical conductivity of MnO_2 nanostructures (10^{-5} - 10^{-6} S cm^{-1}) [26]. Although the electrical conductivity of MnO_2 nanostructures was improved *via* its hybridization with NGNF, the significant impetus on non-enzymatic H_2O_2 sensing performance was not acquired, entailing the acceleration of immense research activities to improve the electrochemical activity of MnO_2 nanostructures [27].

The substitution of 'oxygen' (O) with 'sulfur' (S) in MnO_2 lowers the energy barrier for an efficient electron transfer for the reason of the relatively weaker bond of metal (M)-S compared to that of M – O, facilitating the electrical conductivity of M – S [28]. Furthermore, M – S demonstrates superior physiochemical properties compared to M – O because of its limited variation in volume under harsh electrochemical regimes [29]. Despite the exploitation of MnS nanostructures in dopamine sensing [30], their influences on H_2O_2 electroreduction have not been realized yet. Moreover, MnS suffers with the easier aggregation and confined electron transfer rate [31], which would be swamped with a specific surface engineering of MnS nanostructures in the form of core@shell architectures. In this line, molybdenum sulfide (MoS_2) nanostructures have acquired substantial consideration, owing to its graphene-like layered structure, in which the stacking of three atom layer of S–Mo–S is architectured with the weak van der waals forces, demonstrating the productive features including high electrical conductivity, easier functionalization, large surface area, effectual immobilization on electrodes, and elevated oxidative stability [32,33]. However, the core@shell synergism of MnS@MoS_2 microstructures has not been actualized yet in H_2O_2 detection, which not only confines their electrochemical applications but also prohibits the developmental activities of H_2O_2 sensors.

On the other side, the typical non-enzymatic H_2O_2 detection probes experience certain impediments including the high-priced electrodes and their tiresome pre-treatment and catalyst modification processes, blocked active sites with an inactive binder, and surface poisoning, which cumulatively suppresses the scale-up processes of non-enzymatic H_2O_2 sensors [34,35]. Hence, it is enviable to expand the innovative research strategies for the evolution of time- and cost-efficient electrochemical probes. Additionally, the current diagnostic field requires the miniaturized and bendable sensing devices for on-site applications, urging the advancement of bendable electrochemical probes without any sacrifice in H_2O_2 sensing performance under different bending angles. Accordingly, we report here the development of MnO_2 nanostructures coated tea bag filter paper (TBFP) as a self-standing, bendable, and disposable electrochemical probe for the sensitive and selective H_2O_2 detection and revitalize their role in H_2O_2 electrochemical sensing by converting MnO_2 into MnS and its core@shell architecture configuration with MoS_2 nanostructures.

2. Experimental

2.1. Materials

The succeeding chemicals were inherited from relevant firms and used exclusive of any purification progression: Manganese(II) chloride tetrahydrate ($MnCl_2.4H_2O$, ≥99%, Sisco Research Laboratories), sodium molybdate dihydrate ($Na_2MoO_4.2H_2O$, ≥ 98.5%, Merck), sodium hydroxide (NaOH (pellet), ≥98%, Merck), potassium permanganate ($KMnO_4$, ≥99%, Merck), thiourea (CH_4N_2S, ≥99%, Alfa Aesar), potassium chloride (KOH, ≥99.5%, Merck), uric acid (UA, ≥99%, HPLC, Alfa Aesar), ascorbic acid (AA, ≥99.5%, Alfa Aesar), dopamine (DA, ≥99%, Merck), acetaminophen (AP, ≥99%, Merck), sodium chloride (NaCl, ≥99.5%, Merck), hydrogen peroxide (H_2O_2, 30%, Merck), urea (U, ≥99%, Merck), L-Cysteine (Cys, ≥98%, Merck), L-Leucine (Leu, ≥ 99%, Merck), L-Histidine (Hys, ≥ 99%, Merck), L-Tyrosine (Tyr, ≥98%, Merck), mannose (Man, ≥ 99%, Sigma Aldrich), glutathione (GSH, ≥98%, Merck), sucrose (Suc, ≥99%, Sigma Aldrich), glucose (Glu, ≥99.5%, Sigma Aldrich), fructose (Fru, ≥99%, Sigma Aldrich), sodium nitrate ($NaNO_3$, ≥99%, Sigma Aldrich), sodium sulfate (Na_2SO_4, ≥99%, Sigma Aldrich) etc., The mercantile tea bag filter paper (TBFP) was acquired from local shop and splashed with de-ionized water / ethanol / acetone and dried at 70 °C before use.

2.2. Preparation of MnO_2 nanorods

The hydrothermal treatment of a mixture containing 4 M NaOH and 0.3 M $MnCl_2.4H_2O$ with 30 wt% H_2O_2 was accomplished at 150 °C for 20 h and the ensuing product was rinsed with de-ionized water, dried overnight at 80 °C.

2.3. Preparation of MnS microcubes

The precipitate acquired from the hydrothermal treatment of 0.4 mM MnO_2 with 3.2 mM CH_4N_2S at 180 °C for 20 h was dried for 12 h at 80 °C.

2.4. Preparation of MnS@MoS_2 architectures

The hydrothermal treatment of a mixture containing 0.2 mM $Na_2MoO_4.2H_2O$, MnS dispersion (1 mg ml^{-1}), and 1.5 mM CH_4N_2S at 180 °C for 20 h yielded the MnS@MoS_2 architectures. The obtained product was then gathered *via* centrifugation and dehydrated at 100 °C for 12 h. The weight ratios of 1:1, 2:1, and 3:1 were retained between the MnS and MoS_2 of MnS@MoS_2 architectures.

2.5. Modification of TBFP with processed nanocatalysts

The pre-treated TBFP was drenched into the processed catalyst dispersion (1.5 mg ml^{-1}) and de-moisturized at 80 °C before the electrochemical characterizations. MnO_2, MnS, and MnS@MoS_2

microstructures loaded TBFP are nominated, respectively, as MnO_2/TBFP, MnS/TBFP, and MnS@MoS_2/TBFP and 0.75 mg cm^{-2} catalyst loading was perpetuated for the processed TBFPs (resistance < 10^4 Ω cm^{-1}).

2.6. Material characterizations

Morphological possessions of configured materials were inspected using HITACHI-SU3500 Scanning Electron Microscopy (SEM) and H-9500 Transmission Electron Microscopy (TEM). ARL EQUINOX 100 X-ray diffractometer was applied to appraising the diffraction patterns of processed materials. The structural characterizations of processed materials were acquisitioned with DXR™3 Raman, Nicolet™ iS50 FT-IR, and ESCALAB™ XI X-ray photo electron spectroscopies (XPS). Electrical conductivities of processed materials were scrutinized using Agilent 4156C analyzer.

2.7. Electrochemical characterizations

The electrochemical behaviors of processed TBFPs were probed with CHI-650D electrochemical workstation as reported elsewhere [6]. The amperometric i-t performance of MnS@MoS_2/TBFP was assessed at −0.4 V *vs.* Ag/AgCl against the divergent H_2O_2 concentrations.

3. Results and discussion

The SEM images of processed MnO_2 materials specify the uniformly distributed nanorods with the mean diameter, thickness, and length, respectively, of 560 nm, 170 nm, and several hundred micrometers (Fig. 1a). $Mn(OH)_2$ generated from the reaction between Mn^{2+} and hydroxyl (OH^-) ions is oxidized into MnO_2 nanostructures with the aid of H_2O_2 [36].

$$Mn^{2+} + 2OH^- \rightarrow Mn(OH)_2 \quad (1)$$

$$Mn(OH)_2 + H_2O_2 \rightarrow MnO_2 + 2H_2O \quad (2)$$

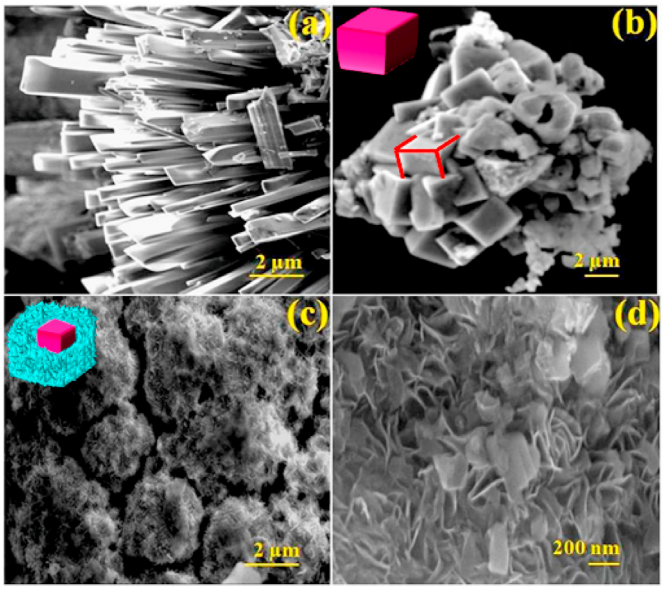

Fig. 1. SEM images of as-prepared (a) MnO_2, (b) MnS, and (c and d) MnS@MoS_2 structures with the insets in (b) and (c) depicting, respectively, the schematic illustration of the MnS, and MnS@MoS_2 structures.

The as-prepared MnS materials demonstrate the cube morphology with a homogeneous size of 2.6 μM (Fig. 1b). Under hydrothermal process at 200 °C, MnO_2 is transferred into Mn_3O_4 with the liberation of O_2 molecule [37]. Hydrogen sulphide (H_2S) produced from the hydrolysis of thiourea combines with Mn_3O_4 and generates MnO, which is prolonged with the sulphidication reaction, yielding the MnS nanostructures [38].

$$3MnO_2 \rightarrow Mn_3O_4 + O_2 \quad (3)$$

$$CH_4N_2S + 2H_2O \rightarrow 2NH_3 + CO_2 + H_2S \quad (4)$$

$$3Mn_3O_4 + H_2S \rightarrow 9MnO + SO_2 + H_2O \quad (5)$$

$$MnO + H_2S \rightarrow MnS + H_2O \quad (6)$$

Under hydrothermal regime, the length of as-prepared nanorods is shortened because of the engaged dissolution process. It is followed by the shoulder to shoulder attachment of shortened nanorods, leading to the formation of microcubes.

On the other side, the SEM images of MnS@MoS_2 architectures reveal that MnS microcubes are homogeneously enveloped with MoS_2 nanosheets and the mean diameter of individual microcubes is enhanced to 3.10 μM, enunciating the 500 nm thickness of MoS_2-shell material. The average thickness and length of individual MoS_2 nanosheet are realized, respectively, as 24 nm and 900 nm (Fig. 1c and d). The highly interconnected MoS_2 nanosheets on MnS-core demonstrate the sizeable and opened "V-type" channels between the adjacent nanosheets, producing the crevices and pores along the nanosheets. The synthesis of MoS_2 is proceeded with the use of Na_2MoO_4 and CH_4N_2S, respectively, as Mo and sulfur sources. The positively charged Mo^{6+} ions are efficaciously adsorbed over the negatively charged S^{2-} of MnS microcubes *via* the electrostatic interaction, proceeded with the chemical reduction of Mo^{6+} into Mo^{4+} and the entangled growth and formation mechanism of MnS@MoS_2 is skeptically illuminated in Fig. S1 [39].

$$4Na_2MoO_4 + 15\ CH_4N_2S + 6H_2O \rightarrow 4MoS_2 + Na_2SO_4 + 6NaSCN + 24NH_3 + 9CO_2 \quad (7)$$

The TEM images of as-prepared MnS@MoS_2 reveal that MnS microcubes are robustly engulfed with the ultrathin MoS_2 nanosheets, demonstrating the typical core@shell architecture. The mean diameter of MnS@MoS_2 architecture and the average thickness and length of enveloped individual MoS_2 sheets are identical with their relevant SEM images (Fig. 2 a-c). The SAED pattern of MnS@MoS_2 divulges the rings and clear spots with the random arrangement, allocating the polycrystalline structure of prepared core@shell material (inset of Fig. 2c). The energy dispersive spectroscopy (EDS) elemental mapping of MnS@MoS_2 exposes the uniform distribution of Mn, Mo, and S, exposing the homogeneous growth of core@shell architecture (Fig. S2).

The reflection planes observed for MnO_2 nanorods including (002), (006), and (119) represent the δ-MnO_2 structure (JCPDS No. 18−0802) (Fig. 3i(a)) [40]. On the other side, the cubic structure of α-MnS is legitimated from the ascertained (111), (200), (220), (311), (222), and (400) reflection planes, respectively, at 29.4, 34.2, 49.3, 58.4, 61.3, and 72.2° (JCPDS No. 06−0518) (Fig. 3i(b)) [41]. Along with the diffraction peaks of MnS, the as-prepared MnS@MoS_2 establishes the distinctive diffraction peaks of MoS_2 at 13.9, 33.4, 39.3, and 58.5°, indexing, respectively, to the (002), (100), (103), and (110) reflection planes of MoS_2's hexagonal structure (JCPDS No. 73−1508) (Fig. 3i(c)) [42].

MnO_2 nanorods reveal the sharp Raman band at 575 cm^{-1}, attributed to the in-plane Mn−O stretching vibrations and its

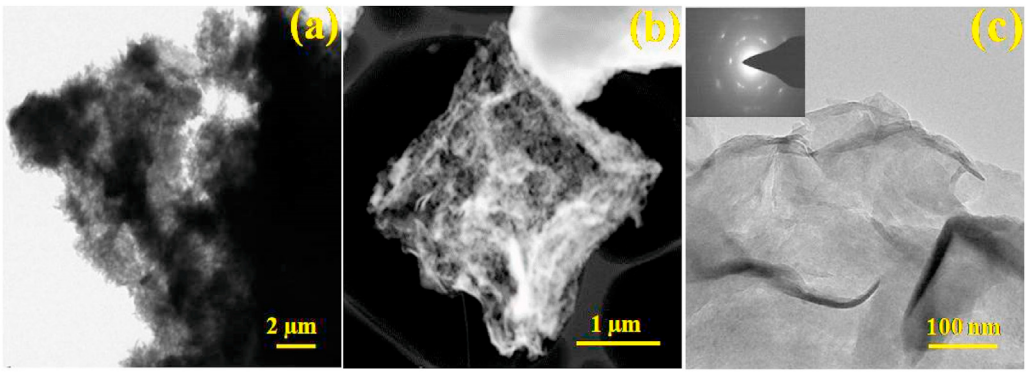

Fig. 2. TEM images of as-prepared MnS@MoS_2 structures.

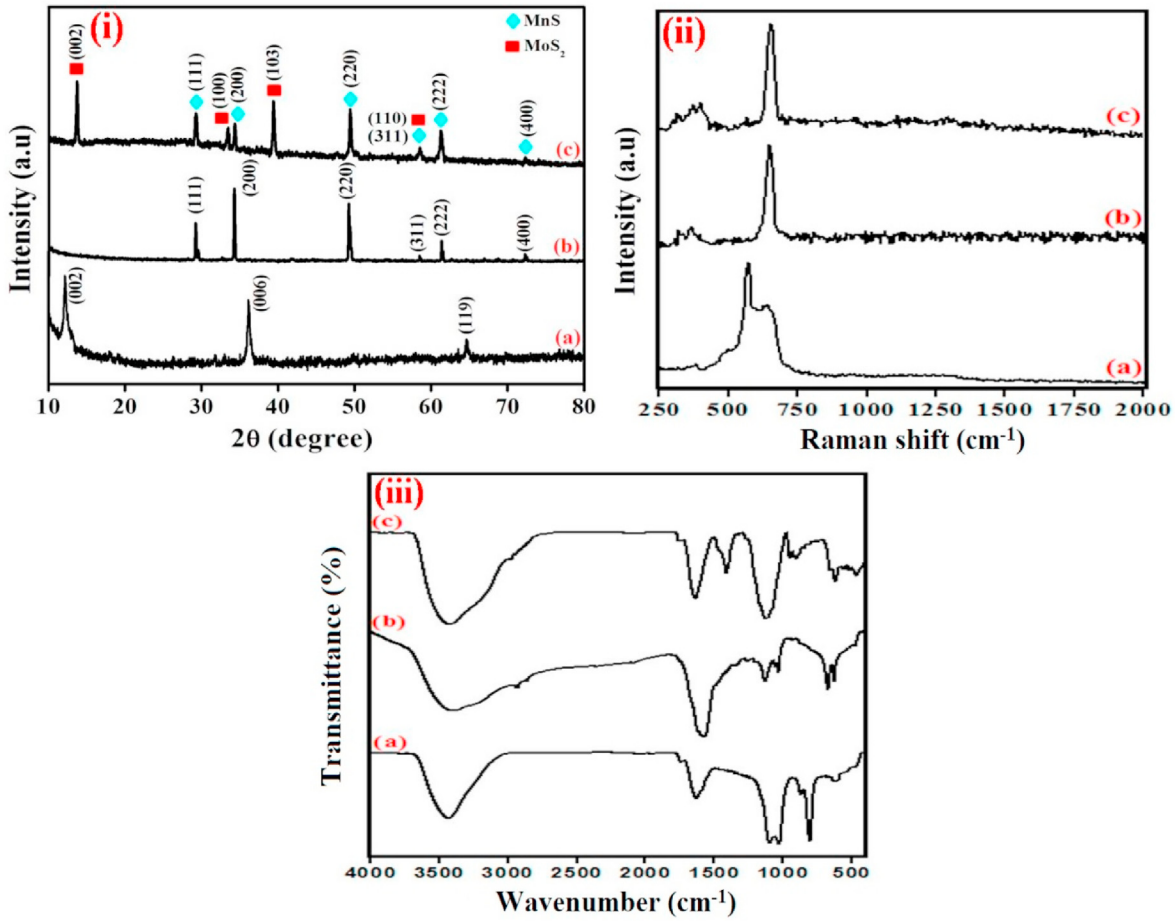

Fig. 3. (i) XRD patterns and (ii) Raman and (iii) FT-IR spectra of (a) MnO_2, (b) MnS, and (c) MnS@MoS_2 structures.

fortified intensity is due to the maximal quadrivalent Mn atoms in the birnessite structure (Fig. 3ii(a)). The bands scrutinized at 504 and 639 cm^{-1} symbolize the out-of-plane Mn—O vibrations and the band at 383 cm^{-1} recognizes the Mn—O stretching mode of the MnO_6 octahedra (Fig. 3ii(a)) [43,44]. For MnS nanostructures, the transverse optical phonon (TO) and longitudinal optical phonon (LO) vibration modes are ascertained, respectively, at 320 and 365 cm^{-1} and the assemblage of TO and LO modes is witnessed at 652 cm^{-1}. (Fig. 3ii(b)) [45]. Together with the characteristic Raman bands of MnS, MnS@MoS_2 demonstrates the MoS_2 Raman bands at 368 and 400 cm^{-1}, mentioning, respectively, in-plane E^1_{2g} and out-of-plane A_{1g} vibrational modes of hexagonal MoS_2 structure, stipulating the establishment of MnS's composite with MoS_2 (Fig. 3ii(c)) [46].

The as-prepared MnO_2 nanorods demonstrate the Mn—O lattice vibration, and surface —OH groups of the Mn-O-Mn bond in MnO_6 octahedral structure, respectively, at 465, 521, and 808 cm^{-1} (Fig. 3iii(a)) [47]. Furthermore, the —OH stretching and bending vibrations of MnO_2 structures are realized, respectively, at 3432 and 1635 cm^{-1} (Fig. 3iii(a)) [48]. The replacement of 'O' with 'S' in MnS microstructures is enunciated from the Mn—S stretching vibration (662 and 613 cm^{-1}) and sulfide co-ordination with Mn (1254 cm^{-1})

(Fig. 3iii(b)) [49]. The adsorption of carbon dioxide from atmosphere on MnS is ascertained with the C—O (1025 cm^{-1}) and C=O stretching vibrations (1561 cm^{-1}) [50]. Core@shell formation of MoS_2 with MnS-core in the form of MnS@MoS_2 is substantiated from the Mo—S stretching vibrations (613 cm^{-1}), S-S bond (903 cm^{-1}), and other MoS_2 related bands (1113 and 1418 cm^{-1}) together with the slightly shifted MnS microstructure's distinctive FT-IR bands (Fig. 3iii(c)) [51].

The as-prepared MnS@MoS_2 manifests Mn 2p, Mo 3d, S 2p, and O 1S peaks in the survey scan XPS spectrum (Fig. 4a). The core-level XPS spectrum of Mn 2p discloses the distinctive peaks at 641.2 and 651.7 eV, imputed, respectively, to the Mn $2p_{3/2}$ and Mn $2p_{1/2}$ (Fig. 4b) [52]. Moreover, the satellite peaks of Mn $2p_{3/2}$ and Mn $2p_{1/2}$ are visualized, respectively, at 644.6 and 657.2 eV (Fig. 4b). The interior level of Mo 3d spectrum deputes two peaks at 229.1 and 232.5 eV, endorsed, respectively, with the Mo $3d_{5/2}$ and Mo $3d_{3/2}$ peak (Fig. 4c) [53]. Moreover, the S 2s peak found at 226.2 eV realizes the oxidation of active S edges. The subsistence of a single doublet in S 2p region coincides with S $2p_{3/2}$ and S $2p_{1/2}$, respectively, at 162.9 and 164.9 eV. The formation of sulfate species *via* the oxidation of sulfur in air is enunciated from the peak at 168.4 eV (Fig. 4d) [54]. The prevailing M-O and oxygen in low coordination at surface are comprehended, respectively, at 530.2 and 531.8 eV in the O 1s spectrum, specifying the prevalence of low level oxygen coordination sites in the surface of MnS@MoS_2 architecture (Fig. 4e) [55].

The electrochemical behavior of processed TBFPs were scrutinized using cyclic voltammograms in 0.1 M NaOH (Fig. 5a) and all of the processed TBFPs demonstrate moderate currents, in which MnS@MoS_2 exemplifies the decipherable current. The electrocatalytic behavior of processed TBFPs towards H_2O_2 reduction was scrutinized using cyclic voltammetry against 5 mM H_2O_2/0.1 M NaOH at 100 mVs^{-1}. Bare TBFP doesn't establish H_2O_2 electroreduction as conspicuous from the obtained voltammogram, related to the inadequate electron mobility paths, and lack of electrochemically responsible sites of TBFP. Upon the surface modification of TBFP with δ-MnO_2 nanorods, the reinforced H_2O_2 electroreduction behavior is witnessed from the moderate

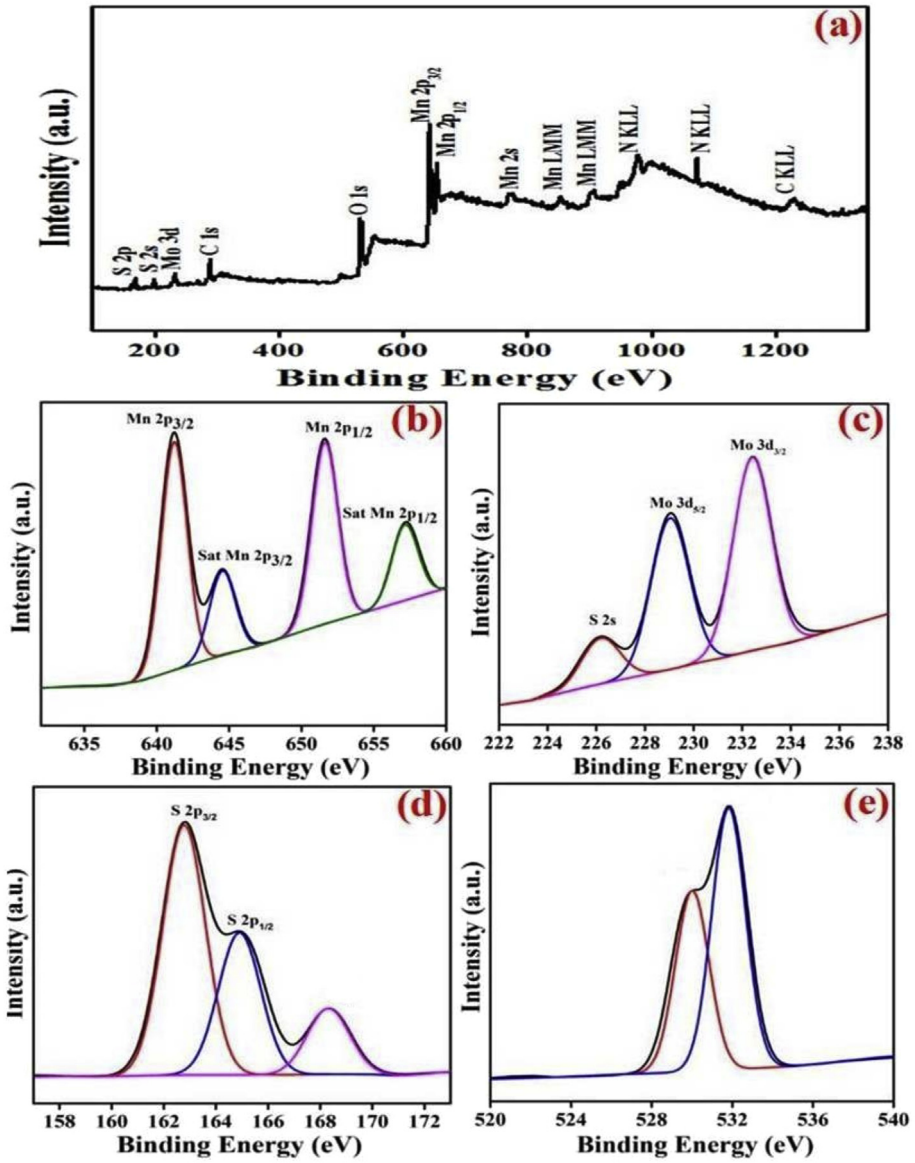

Fig. 4. (a) XPS full scan spectrum of as-prepared MnS@MoS_2 and the de-convoluted spectrum of (b) Mn 2p, (c) Mo3d, (d) S2p, and (e) O1s.

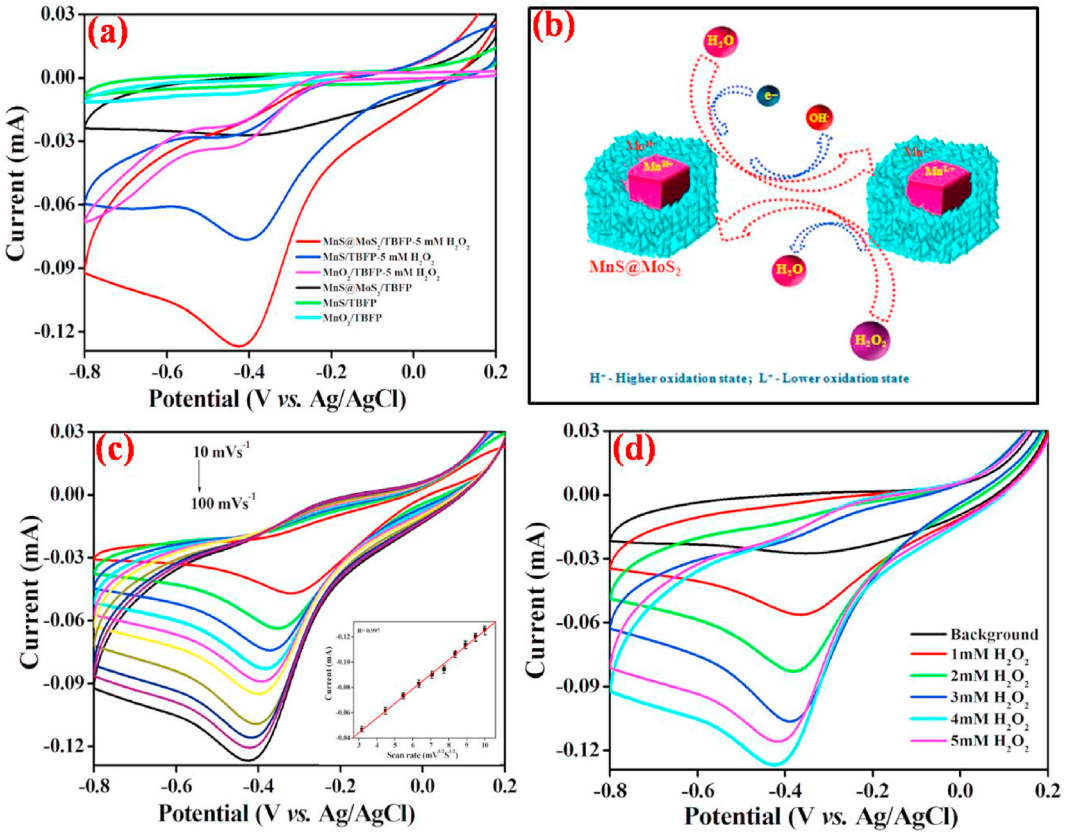

Fig. 5. (a) Voltammograms of processed TBFPs in the deficiency and existence of 5 mM H_2O_2/0.1 M NaOH at of 100 mV s^{-1}, (b) schematic graphics of implicated non-enzymatic H_2O_2 sensing at MnS@MoS_2/TBFP, and voltammograms of MnS@MoS_2/TBFP (c) in 5 mM H_2O_2/0.1 M NaOH as a function of sweep rate (inset pretends a calibration plot of I_{pc} *vs.* square root of the scan rate) and (d) with the accelerated concentration of H_2O_2 in 0.1 M NaOH at 100 mV s^{-1}.

electroreduction peak current *(I_{pc})*. δ-MnO_2 nanorods demonstrate the 2D layered structure with an interlayer separation of ~7 Å [56]. The interlayer gap of δ-MnO_2 nanorods accelerates an effectual accommodation of H_2O_2, which is further promoted with a number of defects and −OH groups and the adsorbed H_2O_2 is electro-reduced at the metallic active centres. Owing to the lower electrical conductivity (2 x 10^{-5} S cm^{-1}) of prepared MnO_2 nanorods, the sluggish H_2O_2 electroreduction kinetics is witnessed at MnO_2/TBFP.

The substitution of 'O' with 'S' in the form of MnS lowers the activation energy barrier because of the weaker bonding of M − S compared to that of M − O, accelerating the electron mobility of MnS microcubes with an improved electrical conductivity of 0.005 S cm^{-1} [9]. Owing to the lower negativity of 'S' compared to 'O', the flexible architecture is realized for MnS, prohibiting the disintegration of chemical structure caused *via* the elongation between layers [57]. The as-prepared MnS microcubes demonstrate the extended porous structures, accelerating the surface accessibility for the mass transportation of H_2O_2. The layered lamellar MnS microstructures provide significant paths for the diffusion of OH^- ions and H_2O_2 molecules in the interlayer region along with the moderate electrochemical stability [58]. It promotes the participation of a number of MnS active sites in the electrolyte/electrode interfacial interaction, directing the moderate electroreduction [59].

The electrocatalytic activity of MnS toward H_2O_2 reduction is further accelerated *via* the core@shell architecture formation of MnS with MoS_2. Amid the processed TBFPs, MnS@MoS_2/TBFP demonstrates the maximum H_2O_2 electroreduction behavior as revealed from the maximal I_{pc} of −0.126 mA at −0.42 V *vs.* Ag/AgCl. 2D MoS_2 demonstrates the typical lamellar structure, comprising of three atomic layers (S—Mo—S), in which one atomic layer of Mo is sandwiched between the two layers of S atoms with the aid of van der Waals interactions [60]. The spacing between the neighborhood layers of MoS_2 is witnessed to be 0.62 nm, which is substantially larger compared to that of graphene (0.35 nm), accelerating the accommodation of H_2O_2 with the maximal analyte utilization efficiency [61,62]. A number of opened V-type pore channels of MoS_2 nanosheets maximize the diffusion of an analyte-H_2O_2 to the MnS-core, facilitating the enlarged and simultaneous contact of H_2O_2 with the core and shell architectures. Moreover, the MoS_2-shell restricts the direct contact of MnS-core with an exterior environment and restricts the loss of active components *via* the selective passage of H_2O_2 and NaOH. On the other side, the exposed edges of MoS_2 sheets serve as that of functionalized graphene sheets, promoting the electrical conductivity of MnS@MoS_2 to 0.01 Scm^{-1}. Thus, the specifically engineered MoS_2-shell not only accelerates the electrical conductivity on the surface of active MnS-core but also stimulates the rapid electron mobility between the electrochemically active centres of MnS@MoS_2 and TBFP. The elastic buffering space offered by the shell confines the considerable expansion and/or contraction of core material under harsh regimes and preserves the surface area and active sites constant throughout the electrochemical reaction. Cumulatively, the hierarchical architecture, core@shell synergism, and preeminent structural aspects of MnS@MoS_2 proffer the maximum H_2O_2 electroreduction at MnS@MoS_2/TBFP.

Initially, the higher oxidation states of metallic active centres generated under the alkaline medium are electrochemically reduced into lower oxidation states. Then, the resultant metallic active centres with lower oxidation states react with the adsorbed

H_2O_2 on the electrode surface, yielding the reduction of H_2O_2 along with the regeneration of metallic active centres with higher oxidation states. Cumulatively, the electrochemical process triggered at a reductive potential effectually converts H_2O_2 into OH^- together with the regeneration of metallic active centres and the proposed mechanism is schemated in Fig. 5b. The above mechanism has been proposed on the bases of obtained electrochemical studies and insights acquired from the published literatures [63,64] and the research works are under progress to elucidate the engaged mechanism with the conclusive evidences. The optimization of core and shell mass ratio in MnS@MoS_2 architecture was scrutinized using voltammograms with their different composition ratios and the relevant result specifies that 2:1 mass ratio of MnS and MoS_2 is favourable for the competent H_2O_2 reduction (Fig. S3).

The engaged H_2O_2 electroreduction kinetics at MnS@MoS_2/TBFP was scrutinized as a function of sweep rate ranging from 10 to 100 mV s^{-1} in 5 mM H_2O_2/0.1 M NaOH (Fig. 5c). A linear function observed for the I_{pc} *vs.* square root of scan rate implies the diffusion controlled progression for the H_2O_2 reduction kinetics at MnS@MoS_2/TBFP (inset of Fig. 5c).

The escalating concentration of H_2O_2 ranging from 1 to 5 mM at 100 mVs^{-1} establishes firm acceleration in reduction current for MnS@MoS_2/TBFP, swamping the antifouling consequences (Fig. 5d).

The realized electrocatalytic studies of MnS@MoS_2 toward H_2O_2 reduction is further extended for non-enzymatic H_2O_2 sensor applications *via* amperometric i-t test against variant H_2O_2 concentrations in 0.1 M NaOH at −0.4 V *vs.* Ag/AgCl (Fig. 6a). A creeping concentration of H_2O_2 in the supporting electrolyte establishes the stair-case related amperogram with the consistent enhancement in amperogram currents for MnS@MoS_2 (Fig. 6a and inset of Fig. 6a). Moreover, the steady state equilibrium for an amperometric H_2O_2 reduction response is actualized at 5s, exposing the rapid response activeness of MnS@MoS_2. The tuned porous architecture and 'V' type channels, respectively, of MnS and MoS_2 manifest the maximum H_2O_2 adsorption, accelerating the utilization efficacy of H_2O_2 at the active centres of a fabricated electrochemical probe [65]. An intimate contact between the core-MnS and shell-MoS_2 and the absence of an insulating binder in TBFP's modification with MnS@MoS_2 confine the internal resistance of a fabricated system and stipulate pathways for the rapid and continuous electron transportation. Thus, the maximum analyte utilization efficacy, homogeneously distributed electrochemically active sites, and composite synergism of MnS@MoS_2 construct the superior non-enzymatic H_2O_2 sensor performances including the lower limit of detection, superior sensitivity, and broad linear range, respectively, of 120 nM, 650 μA mM^{-1} cm^{-2}, and 500 nM - 5 mM (Fig. 6b). The expedience of MnS@MoS_2 in H_2O_2 detection is validated through its surpassed H_2O_2 performances over the pertinent non-enzymatic H_2O_2 sensors reported till date (Table S1). Usually, the implantation of configured electrochemical probes into non-enzymatic H_2O_2 sensor devices is restrained with the ubiquitous impediments of traditional electrodes, such as arduous pre-treatment and polishing, amendment of electrode surface with catalyst slurry, treatment with non-conductive binder, limited electron mobility, detachment of catalysts from electrodes, moderate lifespan, and high

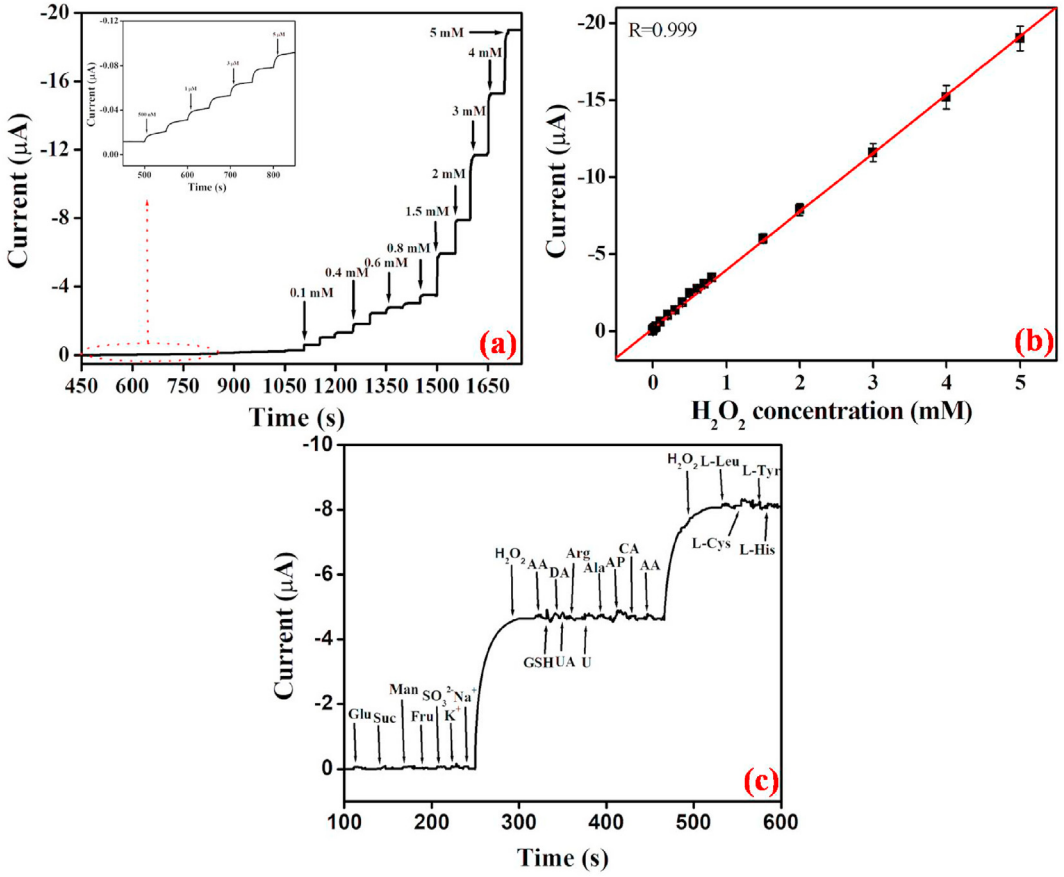

Fig. 6. (a) MnS@MoS_2/TBFP's amperometric activeness against the successive H_2O_2 inclusion in 0.1 M NaOH at −0.4 V vs. Ag/AgCl (inset pretends the i-t profile of MnS@MoS_2/TBFP toward 500 nM - 5 μM H_2O_2), (b) calibration plot of MnS@MoS_2/TBFP's I_{pc} *vs.* H_2O_2 concentration, and (c) interference test of MnS@MoS_2/TBFP with the sequential inclusion of assorted interfering species and H_2O_2 at a concentration of 1.5 mM in 0.1 M NaOH at −0.4 V *vs.* Ag/AgCl.

expenditure. The preceding confinements of traditional electrodes (Table S1) are competently vanquished with the as-configured MnS@MoS_2 modified TBFP (MnS@MoS_2/TBFP). Despite the MnS@MoS_2/TBFP's modest H_2O_2 detection performance in contrast over few endeavors (Table S1), the elementary, low-cost, highly sensitive and selective, and extremely reproducible attributes of MnS@MoS_2/TBFP manifest its formative employment in H_2O_2 detection.

The adequacy of developed electrochemical probe in practical applications is purely dependent upon their anti-interference effect against the existence of other electrochemically active molecules along with H_2O_2 [66]. Accordingly, the selectivity of as-configured MnS@MoS_2/TBFP probe was scrutinized with the amperometric test against the biologically relevant interference species including Glu, Suc, Man, Fru, SO_3^{2-}, Na^+, AA, DA, GSH, UA, U, Arg, Ala, AP, CA, AA, L-Cys, L-Leu, L-Tyr, L-His, and H_2O_2 with a concentration of 1.5 mM at −0.4 V vs. Ag/AgCl (Fig. 6c). The stable amperometric current response was evolved against H_2O_2, while no significant responses were recorded against other interferences. Furthermore, the pre-incorporation of other interferring molecules and ions do not influence the amperometric responses of H_2O_2, signifying exquisite anti-interfering capability of MnS@MoS_2/TBFP on H_2O_2 sensing.

The flexibility of as-configured MnS@MoS_2/TBFP toward H_2O_2 detection was scrutinized with the variant bending angles of 0−180° (Fig. 7a) and the surface area of 2×2 cm^2 was conserved for MnS@MoS_2/TBFP to analyze the flexibility performances. The nullified alteration ascertained in the corresponding CVs and their I_{pc}s under variant bending angles substantiate the excellent flexibility of fabricated MnS@MoS_2/TBFP toward non-enzymatic H_2O_2 detection (Fig. 7a and b).

The authentication of electrochemical stability of MnS@MoS_2/TBFP was scrutinized using amperometric tests against 5 mM H_2O_2/0.1 M NaOH for 60 days. In line with first response, MnS@MoS_2/TBFP conserves 93.3% amperometric performance at 60^{th} day of amperometric test, screening the superior stability of MnS@MoS_2/TBFP (Fig. S4). Moreover, the i-t behavior of eight constructed MnS@MoS_2/TBFPs on H_2O_2 detection demonstrate the relative standard deviation (RSD) of 3.1%, substantiating their superior reproducibility. The repeatability of selfsame constructed MnS@MoS_2/TBFPs with 9 consecutive tests under analogous conditions express the RSD of 2.7%, exposing the satisfactory repeatability of fabricated sensors.

The scale-up probability of processed MnS@MoS_2/TBFP in the evolution of non-enzymatic sensors is articulated from its H_2O_2 content diagnosis in real samples. The pre-regulated concentration of H_2O_2 was mixed with the diluted human urine under alkaline conditions and the quantification of H_2O_2 was scrutinized from their amperometric responses (Table 1). The fabricated probe explicates the appreciable recovery in the range of 98.8−102.4% together with the RSD of 2.18−2.57%, fortifying it's potentiality in H_2O_2 detection.

4. Conclusion

The surface engineering modification of MnS microcubes with MoS_2 was accomplished in the form of core@shell architectures *via* a simple hydrothermal technique. The resultant MnS@MoS_2 structures were effectively loaded on TBFP (MnS@MoS_2/TBFP) and used as an electrochemical probe for non-enzymatic H_2O_2 detection. The constricts linked with the current non-enzymatic H_2O_2 sensor probes including time- and cost-consumed cleaning and catalyst modification protocols of electrochemical probes and exploitation of insulating binders were efficaciously engulfed with the as-configured MnS@MoS_2/TBFP. The prevailed open 'V' type channels on MoS_2 shell architecture allow the diffusion of H_2O_2 into the core-MnS architecture and maximize the analyte utilization efficacy, accelerating the mass transport of ions/electrons with lower resistance. The synergism of multiform metal structures, considerable electrical conductivity, and consistent active sites positioning of MnS@MoS_2 efficaciously electroreduce H_2O_2, concreting the sensitive and selective H_2O_2 detection in real sample diagnosis. Thus, the as-configured MnS@MoS_2/TBFP not only realizes the employment of well tuned core@shell architectures in electrocatalytic reduction of H_2O_2 but also opens new epitomes in the progression of economical and flexible electrochemical probe

Table 1
Non-enzymatic H_2O_2 diagnosis in human urine samples at MnS@MoS_2/TBFP.

H_2O_2 added (μM)	H_2O_2 found (mM)	RSD[b] (%)	Recovery (%)
10	9.88	2.31	98.8
20	20.44	2.18	102.2
30	30.54	2.25	101.8
40	40.76	2.57	101.9
50	51.24	2.33	102.4

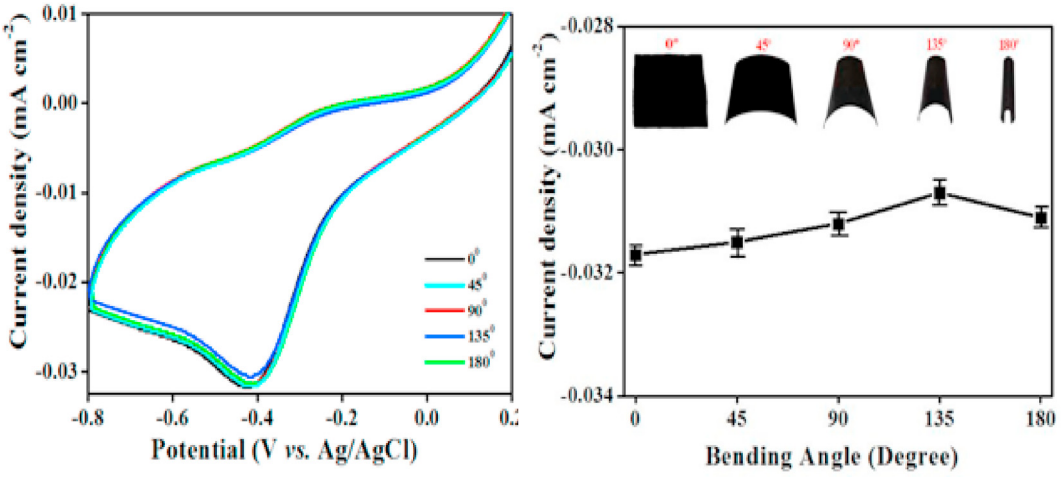

Fig. 7. (a) Voltammograms of MnS@MoS_2/TBFP at assorted bending angles with 5 mM H_2O_2/0.1 M NaOH at 100 mV s^{-1}, and (b) the related I_{pc} *vs.* assorted bending angles of MnS@MoS_2/TBFP (inset pretends the photographs of MnS@MoS_2/TBFP at assorted bending angles).

for non-enzymatic H_2O_2 detection.

CRediT authorship contribution statement

N. Priyanga: Conceptualization, Methodology, Software. **A. Sahaya Raja:** Data curation, Writing - original draft. **Mehboobali Pannipara:** Visualization, Investigation. **Abdullah G. Al-Sehemi:** Formal analysis. **Siew-Moi Phang:** Writing - original draft. **Yang Xia:** Formal analysis, Investigation. **Shu-Yi Tsai:** Methodology, Software. **J. Annaraj:** Formal analysis, Software. **S. Sambathkumar:** Formal analysis. **G. Gnana kumar:** Funding acquisition, Writing - review & editing.

Declaration of competing interest

The authors declare that they have no known competing financial interests or personal relationships that could have appeared to influence the work reported in this paper.

Acknowledgement

This research effort was supported by the Department of Science and Technology, New Delhi Major Project Grant No.: DST/TMD/HFC/2K18/52(C). The authors extend their appreciation to the Deanship of Scientific Research at King Khalid University for funding this work through Research Group Project under grant number R.G.P.1/177/41.

Appendix A. Supplementary data

Supplementary data to this article can be found online at https://doi.org/10.1016/j.jallcom.2020.157103.

References

[1] Y. Kofuji, Y. Isobe, Y. Shiraishi, H. Sakamoto, S. Tanaka, S. Ichikawa, T. Hirai, Carbon nitride-aromatic diimide-graphene nanohybrids: metalfree photocatalysts for solar-to-hydrogen peroxide energy conversion with 0.2% efficiency, J. Am. Chem. Soc. 138 (2016) 10019−10025.
[2] C.F. Nathan, S.C. Silverstein, L.H. Brukner, Z.A. Cohn, Extracellular cytolysis by activated macrophages and granulocytes. II. hydrogen peroxide as a mediator of cytotoxicity, J. Exp. Med. 149 (1979) 100−113.
[3] S.A.M. Shaeg, S.M.M. Ehteshami, S.H. Chan, N.T. Nguyen, S.N. Tan, Membraneless hydrogen peroxide micro semi-fuel cell for portable applications, RSC Adv. 4 (2014) 37284−37287.
[4] J. Meier, E.M. Hofferber, J.A. Stapleton, N.M. Iverson, Hydrogen peroxide sensors for biomedical applications, Chemosensors 7 (1−11) (2019) 64.
[5] W. Chen, S. Cai, Q.Q. Ren, W. Wen, Y.D. Zhao, Recent advances in electrochemical sensing for hydrogen peroxide: a review, Analyst 137 (2012) 49−58.
[6] C. Karthikeyan, K. Ramachandran, S. Sheet, D.J. Yoo, Y.S. Lee, Y.S. Kumar, A.R. Kim, G.G. kumar, Pigeon-excreta-mediated synthesis of reduced graphene oxide (rGO)/$CuFe_2O_4$ nanocomposite and its catalytic activity toward sensitive and selective hydrogen peroxide detection, ACS Sustain. Chem. Eng. 5 (2017) 4897−4905.
[7] G. Amala, J. Saravanan, D.J. Yoo, A.R. Kim, G.G. kumar, An environmentally benign one pot green synthesis of reduced graphene oxide based composites for the enzyme free electrochemical detection of hydrogen peroxide, New J. Chem. 41 (2017) 4022−4030.
[8] K.J. Babu, S. Sheet, Y.S. Lee, G.G. kumar, Three-dimensional dendrite Cu-Co/reduced graphene oxide architectures on a disposable pencil graphite electrode as an electrochemical sensor for nonenzymatic glucose detection, ACS Sustain. Chem. Eng. 6 (2018) 1909−1918.
[9] K.J. Babu, T.R. kumar, D.J. Yoo, S.M. Phang, G.G. kumar, Electrodeposited nickel cobalt sulphide flower-like architectures on disposable cellulose filter paper for enzyme free glucose sensor applications, ACS Sustain. Chem. Eng. 6 (12) (2018) 16982−16989.
[10] G. Shan, S. Zheng, S. Chen, Y. Chen, Y. Liu, Detection of label-free H2O2 based on sensitive Au nanorods as sensor, Colloids Surf., B 102 (2013) 327−330.
[11] Z. Miao, D. Zhang, Q. Chen, Non-enzymatic hydrogen peroxide sensors based on multi-wall carbon nanotube/pt nanoparticle nanohybrids, Materials 7 (2014) 2945−2955.
[12] S. Bozkurt, B. Tosun, B. Sen, S. Akocak, A. Savk, M.F. Ebeoğlugil, F. Sen, A hydrogen peroxide sensor based on TNM functionalized reduced graphene oxide grafted with highly monodisperse Pd nanoparticles, Anal. Chim. Acta 989 (2017) 88−94.
[13] M. Guler, V. Turkoglu, A. Bulut, M. Zahmakiran, Electrochemical sensing of hydrogen peroxide using Pd@Ag bimetallic nanoparticles decorated functionalized reduced graphene oxide, Electrochim. Acta 263 (2018) 118−126.
[14] M.J. Songa, S.W. Hwanga, D. Whanga, Non-enzymatic electrochemical CuO nanoflowers sensor for hydrogen peroxide detection, Talanta 80 (2010) 1648−1652.
[15] Y. Liu, L. Wang, L. Yang, Y. Zhan, L. Zou, B. Ye, Nonenzymatic H_2O_2 electrochemical sensor based on SnO_2-NPs coated polyethylenimine functionalized graphene, Electroanalysis 29 (2017) 1−10.
[16] D.S. achari, C. Santhosh, R. Deivasegamani, R. Nivetha, A. Bhatnagar, S.K. Jeong, A.N. Grace, A non-enzymatic sensor for hydrogen peroxide based on the use of α-Fe_2O_3 nanoparticles deposited on the surface of NiO nanosheets, Microchim. Acta 184 (2017) 3223−3229.
[17] A. Din, S.B. Khan, M.I. Khan, S.A.B. Asif, M.A. Khan, S. Gul, K. Akhtar, A.M. Asiri, Cadmium oxide based efficient electrocatalyst for hydrogen peroxide sensing and water oxidation, J. Mater. Sci. Mater. Electron. 28 (2017) 1092−1100.
[18] M. Wang, X. Jiang, J. Liu, H. Guo, C. Liu, Highly sensitive H_2O_2 sensor based on Co_3O_4 hollow sphere prepared via a template-free method, Electrochim. Acta 182 (2015) 613−620.
[19] W. Liu, H. Zhang, B. Yang, Z. Li, L. Lei, X. Zhang, A Non-enzymatic hydrogen peroxide sensor based on vertical nio nanosheets supported on the graphite sheet, J. Electroanal. Chem. 749 (2015) 62−67.
[20] J.H. Lee, H.G. Hong, Nonenzymatic electrochemical sensing of hydrogen peroxidebased on a polyaniline-MnO $_2$ nanofiber-modified glassy carbon electrode, J. Appl. Electrochem. 45 (2015) 1153−1162.
[21] J. Wang, M. Xu, R. Zhao, G. Chen, A highly sensitive H_2O_2 sensor based on zinc oxide nanorod arrays film sensing interface, Analyst 135 (2010) 1992−1996.
[22] J. Hu, F. Qian, G. Song, W. Li, L. Wang, Ultrafine MnO_2 nanowire arrays grown on carbon fibers for high-performance supercapacitors, Nanoscale Res. Lett. 11 (2016) 4691−4696.
[23] T.N. Lambert, J.A. Vigil, S.E. White, C.J. Delker, D.J. Davis, M. Kelly, M.T. Brumbach, M.A. Rodriguez, B.S. Swartzentruber, Understanding the effects of cationic dopants on α-mno_2 oxygen reduction reaction electrocatalysis, J. Phys. Chem. C 121 (5) (2017) 2789−2797.
[24] A. Kumar, M.S. Aathira, U. Pal, S.L. Jain, Photochemical oxidative coupling of 2-naphthols using hybrid rGO/MnO_2 nanocomposite under visible light irradiation, ChemCatChem 108 (2018) 1844−1852.
[25] L. Wang, M. Deng, G. Ding, S. Chen, F. Xu, Manganese dioxide based ternary nanocomposite for catalytic reduction and nonenzymatic sensing of hydrogen peroxide, Electrochim. Acta 114 (2013) 416−423.
[26] K.J. Babu, A. Zahoor, K.S. Nahm, R. Ramachandran, M.A.J. Rajan, G.G. kumar, The influences of shape and structure of MnO_2 nanomaterials over the nonenzymatic sensing ability of hydrogen peroxide, J. Nanopart. Res. 16 (2014) 2250, 1-10.
[27] K. Ramachandran, A. Zahoor, T.R. Kumar, K.S. Nahm, A. Balasubramani, G.G. Kumar, MnO_2 nanorods grown NGNF nanocomposites for the application of highly sensitive and selective electrochemical detection of hydrogen peroxide, J. Ind. Eng. Chem. 46 (2017) 19−27.
[28] Y. Pei, C. Liu, Z. Han, Z.G. Neale, W. Qian, S. Xiong, Z. Jiang, G. Cao, Revealing the impacts of metastable structure on the electrochemical properties: the case of MnS, J. Power Sources 431 (2019) 75−83.
[29] C. Liu, Z.G. Neale, G.Z. Cao, Understanding electrochemical potentials of cathodematerials in rechargeable batteries, Mater. Today 19 (2) (2016) 109−123.
[30] S. Ramki, K. Pandi, S.M. Chen, Y.T. Ye, T.W. Chen, Q. Hao, Hydrothermal synthesis of manganese sulfide decorated graphene oxide for effective electrochemical sensing of dopamine, Int. J. Electrochem. Sci. 14 (2019) 1069−1081.
[31] S. He, W. Qiu, L. Wang, F. Gao, W. Wang, Z. Hu, Q. Wang, Hollow MnS nanospheres as electron transfer promoters of hemoglobin and their electrochemical sensing applications, J. Mater. Sci. 51 (2016) 7156−7169.
[32] S. Lee, Y.K. Kim, J.Y. Hong, J. Jang, Electro-response of MoS_2 nanosheets-based smart fluid with tailorable electrical conductivity, ACS Appl. Mater. Interfaces 8(36)(2016) 24221-24229.
[33] G.A.M. Ali, M.R. Thalji, W.C. Soh, H. Algarni, K.F. Chong, One-step electrochemical synthesis of MoS_2/graphene composite for supercapacitor application, J. Solid State Electr. 24 (2020) 25−34.
[34] K. Vasuki, K.J. Babu, S. Sheet, G. Siva, A.R. Kim, D.J. Yoo, G.G. kumar, Amperometric hydrogen peroxide sensor based on the use of $CoFe_2O_4$ hollow nanostructures, Microchim. Acta 184 (2017) 2579−2586.
[35] G. Yu, W. Wu, X. Pan, Q. Zhao, X. Wei, Q. Lu, High sensitive and selective sensing of hydrogen peroxide released from pheochromocytoma cells based on pt-au bimetallic nanoparticles electrodeposited on reduced graphene sheets, Sensors 15 (2015) 2709−2722.
[36] L. Lan, G. Gu, Q. Li, H. Zhang, K. Xu, B. Liua, B. Liu, Manganese oxide nanostructures: low-temperature selective synthesis and thermal conversion, RSC Adv. 5 (2015) 25250−25257.
[37] D.P.M.D. Shaik, P. Rosaiah, O.M. Hussain, Electrical and electrochemical performance of Mn_3O_4 nanoparticles synthesized by hydrothermal method, AIP Conf. Proc. 1728 (1−6) (2016), 020501.
[38] S.H. Chaki, S.M. Chauhana, J.P. Tailor, M.P. Deshpande, Synthesis of manganese sulfide (MnS) thin films by chemical bath deposition and their characterization, J. Mater. Res. Technol. 6 (2) (2017) 123−128.
[39] X.L. Li, Y.D. Li, MoS_2 Nanostructures: synthesis and electrochemical Mg^{2+} intercalation, J. Phys. Chem. B 108 (37) (2004) 13893−13900.

[40] L. Ma, N. Meng, Y. Zhang, F. Lian, Improved electrocatalytic activity of δ-MnO_2@MWCNTs by inducing the oriented growth of oxygen reduction products in Li-O_2 batteries, Nano Energy 58 (2019) 508–516.
[41] T. Chen, U. Rajaji, S. Chen, Y. Li, R.J. Ramalingam, Ultrasound-assisted synthesis of α-MnS (alabandite) nanoparticles decorated reduced graphene oxide hybrids: enhanced electrocatalyst for electrochemical detection of Parkinson's disease biomarker, Ultrason. Sonochem. 56 (2019) 378–385.
[42] Z. Zheng, S. Cong, W. Gong, J. Xuan, G. Li, W. Lu, F. Geng, Z. Zhao, Semiconductor SERS enhancement enabled by oxygen incorporation, Nat. Commun. 8 (2017) 1–10, 1993.
[43] Z.M. Chana, D.A. Kitchaev, J.N. Weker, C. Schnedermann, K. Lim, G. Ceder, W. Tumas, M.F. Toney, D.G. Nocera, Electrochemical trapping of metastable Mn3+ ions for activation of MnO2 oxygen evolution catalysts, Proc. Natl. Acad. Sci. 115 (23) (2017) E5261–E5268.
[44] B. Yin, S. Zhang, H. Jiang, F. Qu, X. Wu, Phase-controlled synthesis of polymorphic MnO2 structures for electrochemical energy storage, J. Mater. Chem. A 3 (2015) 5722–5729.
[45] M. Girish, T. Dhandayuthapani, R. Sivakumar, C. Sanjeeviraja, M. Kumaresavanji, Substrate temperature and molar ratio induced changes on the properties of nebulized spray deposited MnS films, J. Mater. Sci. Mater. Electron. 28 (2017) 6741–6753.
[46] R. Thangappan, S. Kalaiselvam, A. Elayaperumal, R. Jayavel, M. Arivanandhan, R. Karthikey, Y. Hayakawa, Graphene decorated with MoS_2 nanosheets a synergetic energy storage composite electrode for supercapacitor applications, Dalton Trans. 45 (2016) 2637–2646.
[47] H. Wang, Y. Wang, Y. Sun, X. Pan, D. Zhang, Y.F. Tsang, Differences in Sb(V) and As(V) adsorption onto a poorly crystalline phyllomanganate (δ-MnO_2): adsorption kinetics, isotherms, and mechanisms, Process Saf. Environ. 113 (2018) 40–47.
[48] D. Ghosh, S. Bhandari, D. Khastgir, Synthesis of MnO_2 nanoparticle and its effective utilization as UV protector for outdoor high voltage polymeric insulator used in power transmission line, Phys. Chem. Chem. Phys. 18 (2016) 32876–32890.
[49] T. Dhandayuthapani, M. Girish, R. Sivakumar, C. Sanjeeviraja, R. Gopalakrishnan, Tuning the morphology of metastable MnS films by simple chemical bath deposition technique, Appl. Surf. Sci. 353 (2015) 449–458.
[50] S.S. Rao, I.K. Durga, B. Naresh, B. Jin-Soo, T.N.V. Krishna, C. In-Ho, J. Ahn, H. Kim, One-pot hydrothermal synthesis of novel Cu-MnS with PVP cabbage-like nanostructures for high performance supercapacitors, Energies 11 (1–14) (2018) 1590.
[51] W. Feng, L. Chen, M. Qin, X. Zhou, Q. Zhang, Y. Miao, K. Qiu, Y. Zhang, C. He, Flower-like PEGylated MoS2 nanoflakes for near-infrared photothermal cancer therapy, Sci. Rep 5 (2015), 17422(1-13).
[52] Y. Ma, Y. Ma, G. Kim, T. Diemant, R.J. Behm, D. Geiger, U. Kaiser, A. Varzi, S. Passerini, Superior lithium storage capacity of α-MnS nanoparticles embedded in s-doped carbonaceous mesoporous frameworks, Adv. Energy Mater. 9 (43) (2019) 1902077, 1-15.
[53] D. Dinda, M.E. Ahmed, S. Mandal, B. Mondal, S.K. Saha, Amorphous molybdenum sulfide quantum dots: an efficient hydrogen evolution electrocatalyst in neutral medium, J. Mater. Chem. 4 (2016) 15486–15493.
[54] G. Li, J. Sun, W. Hou, S. Jiang, Y. Huang, J. Geng, Three-dimensional porous carbon composites containing high sulfur nanoparticle content for high-performance lithium–sulfur batteries, Nat. Commun 7 (2016), 10601(1-10).
[55] K. Xiao, L. Xia, G. Liu, S. Wang, L. Ding, H. Wang, Honeycomb-like $NiMoO_4$ ultrathin nanosheet arrays for high-performance electrochemical energy storage, J. Mater. Chem. 3 (2015) 6128–6135.
[56] X. Li, H. Zhu, Two-dimensional MoS_2: properties, preparation, and applications, J. Materiomics. 1 (2015) 33–44.
[57] S. Devaraj, N. Munichandraiah, Effect of crystallographic structure of MnO_2 on its electrochemical capacitance properties, J. Phys. Chem. C 112 (2008) 4406–4417.
[58] D. Li, Y. Gong, C. Pan, Facile synthesis of hybrid CNTs/$NiCo_2S_4$ composite for high performance supercapacitors, Sci. Rep. 6 (1–7) (2016) 29788.
[59] P. Tiwari, G. Malik, R. Chandra, Phase-dependent structural and electrochemical properties of single crystalline MnS thin films deposited by DC reactive sputtering, J. Appl. Phys. 124 (1–12) (2018) 195106.
[60] K. Ma, A. Sinha, X. Dang, H. Zhao, Electrochemical preparation of gold nanoparticles-polypyrrole co-decorated 2D MoS_2 nanocomposite sensor for sensitive detection of glucose, J. Electrochem. Soc. 166 (2) (2019) B147–B154.
[61] G. Jeevanandham, R. Jerome, N. Murugan, M. Preethika, K. Vediappan, A.K. Sundramoorthy, Nickel oxide decorated MoS_2 nanosheet based non-enzymatic sensor for the selective detection of glucose, RSC Adv. 10 (2020) 643–654.
[62] S. Shanthi, H. Ikeda, I.M. Patil, B. kakade, Y. Hayakawa, S. Ponnusamy, C. Muthamizhchelvan, Hierarchical MoS_2 nanosheets - $FeCo_2O_4$ nanowires on flexible carbon cloth substrate for high-performance flexible supercapacitors, Int. J. Electrochem. Sci. 14 (2019) 5535–5546.
[63] Y. Pan, W. Yi, Z. Hou, Y. Liu, Green and large-scale one-pot synthesis of small-sized graphene-bridged manganese dioxide nanowire network as new electrode material for electrochemical sensing, J. Sol. Gel Sci. Technol. 76 (2015) 341–348.
[64] D. Ye, H. Li, G. Liang, J. Luo, X. Zhang, S. Zhang, H. Chen, J. Kong, A three dimensional hybrid of MnO_2/graphene/carbon nanotubes based sensor for determination of hydrogen-peroxide in milk, Electrochim. Acta 109 (2013) 195–200.
[65] N. Senthilkumar, G.G. kumar, A. Manthiram, 3D Hierarchical core–shell nanostructured arrays on carbon fibers as catalysts for direct urea fuel cells, Adv. Energy Mater. 8 (6) (2017) 1702207, 1-12.
[66] G.G. kumar, K.J. Babu, K.S. Nahm, Y.J. Hwang, A facile one-pot green synthesis of reduced graphene oxide and its composites for nonenzymatic hydrogen peroxide sensor applications, RSC Adv. 4 (2014) 7944–7951.